

Automated design of nonreciprocal thermal emitters via Bayesian optimization

Bach Do,^{†,¶} Sina Jafari Ghalekohneh,^{‡,¶} Taiwo Adebiyi,[†] Bo Zhao,^{*,‡} and Ruda Zhang^{*,†}

[†]*Department of Civil and Environmental Engineering, University of Houston, Houston, TX 77204, USA*

[‡]*Department of Mechanical and Aerospace Engineering, University of Houston, Houston, TX 77204, USA*

[¶]*These authors contributed equally to this work.*

E-mail: bzhao8@uh.edu; rudaz@uh.edu

Abstract

Nonreciprocal thermal emitters that break Kirchhoff’s law of thermal radiation promise exciting applications for thermal and energy applications. The design of the bandwidth and angular range of the nonreciprocal effect, which directly affects the performance of nonreciprocal emitters, typically relies on physical intuition. In this study, we present a general numerical approach to maximize the nonreciprocal effect. We choose doped magneto-optic materials and magnetic Weyl semimetal materials as model materials and focus on pattern-free multilayer structures. The optimization randomly starts from a less effective structure and incrementally improves the broadband nonreciprocity through the combination of Bayesian optimization and reparameterization. Optimization results show that the proposed approach can discover structures that can achieve broadband nonreciprocal emission at wavelengths from 5 to 40 μm

using only a fewer layers, significantly outperforming current state-of-the-art designs based on intuition in terms of both performance and simplicity.

Keywords: Nonreciprocity, Thermal emitters, Gaussian process, Bayesian optimization, Reparameterization

1 Introduction

2 Over the past two decades, the control of thermal radiation transfer has gained significant
3 interest due to its vital applications in spacecraft, manufacturing, thermal management, and
4 energy conversion.^{1–4} Typically, the design and simulation of these systems assume reci-
5 procity. According to Kirchhoff’s law,^{5,6} for reciprocal thermal emitters, emissivity (ε) and
6 absorptivity (α) are equal for a given direction, frequency, and polarization. This reciprocal
7 relationship between emission and absorption represents a significant constraint on control-
8 ling the radiative heat flow,^{7,8} and prevents radiative energy harvesting technologies from
9 reaching their thermodynamic limits.^{9–14}

10 Recent research advances^{2,15–17} have suggested that reciprocity is not a requirement of
11 thermodynamics, and it breaks down for nonreciprocal thermal emitters which allow ε and α
12 to be separately controlled. Nonreciprocal thermal emission provides the pathway to record-
13 breaking high-efficiency radiative energy harvesting techniques,^{9,13,14,18–20} thermal regulation
14 systems,^{21–24} and mechanical propulsion with radiative heat flow.^{25,26} Importantly, to achieve
15 the ultimate performance in these applications, especially for far-field scenarios, nonrecip-
16 rocal thermal radiative properties should be achieved over a broad wavelength and angu-
17 lar range. Designing nonreciprocal structures with desired properties is a new challenge
18 compared to designing reciprocal emitters,^{27,28} since one needs to codesign emissivity and
19 absorptivity simultaneously.

20 Early work has demonstrated that enhanced nonreciprocal properties^{16,29} could be ob-
21 tained in semiconductors and semimetals at the excitation of resonances in the wavelength

range where the dielectric function crosses zero (i.e., epsilon-near-zero or ENZ range). Based on this principle, current approaches to achieving broadband nonreciprocity rely on multilayered structures in which each layer exhibits strong nonreciprocity at a different ENZ wavelength. Combined, the structure can trigger a number of these resonances simultaneously and yield broadband nonreciprocity. For example, Liu et al.²² demonstrated broadband nonreciprocal emission at wavelengths from 20 to 40 μm using a gradient-doped multilayer InAs structure, where each layer shows strong nonreciprocity at a specific resonance wavelength under an external magnetic field. Similarly, Zhang and Zhu³⁰ proposed broadband nonreciprocity at wavelengths from 10 to 20 μm using a multilayer magnetic Weyl semimetal structure with a gradient chemical potential. However, since the material and the associated parameters, like carrier concentration and geometric parameters, can all be free to choose, designing high-performance structures of this kind is quite challenging and typically relies on physical intuition. As a result, the final designs are oftentimes suboptimal; for example, requiring a high number of layers that are challenging to fabricate. Additionally, current studies usually focus on optimizing the absolute value of the contrast between emissivity and absorptivity.³¹ We make sure the sign of the contrast is respected in the design algorithm since it is crucial to the direction of photon transport³² and can be important in various applications where the net photon flow direction is significant.^{13,33} Despite the effectiveness of multilayer structures in achieving broadband nonreciprocal thermal emission, an effective approach to optimize the performance is lacking.

Here we propose a numerical method based on Bayesian optimization (BO)³⁴⁻³⁹ and reparameterization to optimize thermal emitters with a large number of design parameters and high computational cost. BO is selected because it can address the high computational demand presented by repeated calculations of absorptivity and emissivity during the optimization process, which hinders the use of any population-based optimizers,^{27,40} gradient-based optimizers,⁴¹ or data-driven approaches requiring a large dataset.^{28,42} The reparameterization imposes user-defined constraints on the structures' profiles and further

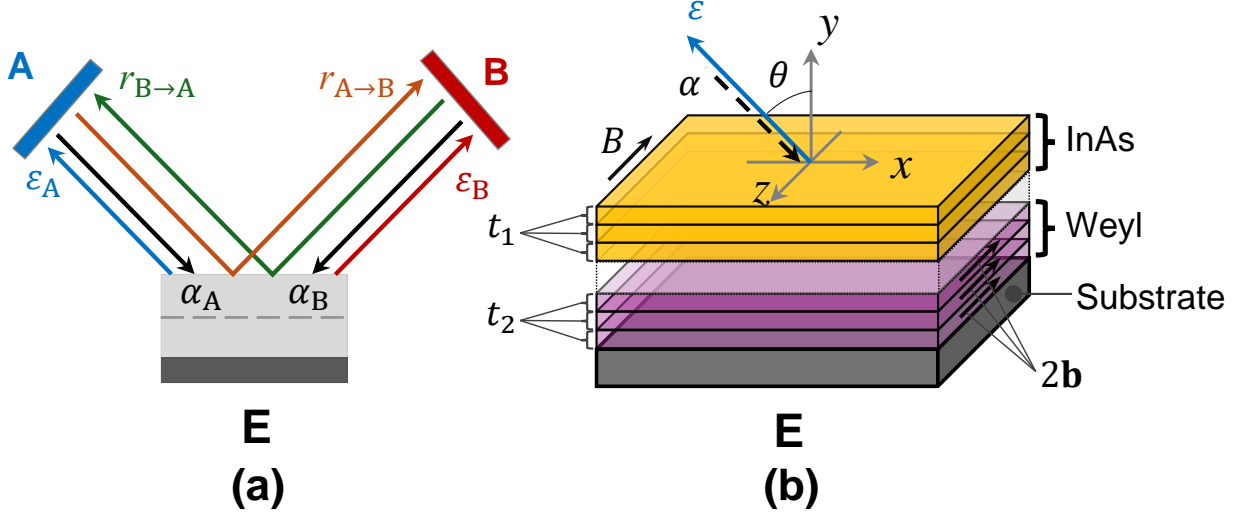


Figure 1: (a) Illustration of radiative heat exchange between two blackbodies (A and B) and an emitter (E) under thermal equilibrium. (b) Illustration of a multilayer structure consisting of InAs layers on top of Weyl semimetal layers on a reflective substrate.

reduces the number of optimization parameters, thereby reinforcing the efficiency of BO which is well-suited for small to medium optimization problems.³⁸ Our optimization approach is applicable to both reciprocal and nonreciprocal emitters. In this work, we focus on demonstrating its application in achieving enhanced broadband nonreciprocal radiative properties with the sign of the contrast being maintained. We aim to find structures with a much fewer number of layers and yet can achieve nonreciprocity in an even broader wavelength range than current designs.

Absorptivity and emissivity of nonreciprocal emitters

For opaque structures, the emissivity and absorptivity can be computed from the reflectivity, as discussed in previous studies.^{43,44} Here, we briefly review the rationale behind the approach to facilitate our later discussion. Consider a system in thermal equilibrium that consists of an opaque thermal emitter (E) exchanging energy with two blackbodies, A and B, (Fig. 1(a)). The emission from blackbody A is either absorbed by the thermal emitter E (α_A), or reflected

and absorbed by blackbody B ($r_{A \rightarrow B}$), leading to the following relationship:

$$\alpha_A + r_{A \rightarrow B} = 1, \quad (1)$$

where α_A represents the absorptivity in direction A at a specific wavelength, and $r_{A \rightarrow B}$ is the reflectivity from A to B at that wavelength.

Moreover, each blackbody absorbs and emits an equal amount of energy at thermal equilibrium, resulting in

$$\varepsilon_A + r_{B \rightarrow A} = 1, \quad (2)$$

Combining Eqs. (1) , and (2), we have

$$\alpha_A - \varepsilon_A = r_{B \rightarrow A} - r_{A \rightarrow B}. \quad (3)$$

For reciprocal emitters with $r_{A \rightarrow B} = r_{B \rightarrow A}$,⁴⁵ it follows that $\alpha_A = \varepsilon_A$, which is consistent with Kirchhoff's law of radiation.⁴⁶ However, for nonreciprocal emitters, we have $r_{A \rightarrow B} \neq r_{B \rightarrow A}$,⁴³ and thus $\alpha_A \neq \varepsilon_A$, which violates Kirchhoff's law of radiation. The absorptivity and emissivity are given as

$$\begin{aligned} \alpha_A &= 1 - r_{A \rightarrow B}, \\ \varepsilon_A &= 1 - r_{B \rightarrow A}. \end{aligned} \quad (4)$$

For linear and static thermal emitters we consider here,^{47,48} one needs to start with a material that breaks the reciprocity to obtain nonreciprocal thermal radiation. Magneto-optical material InAs^{22,29,43,49} and magnetic Weyl semimetals^{16,50–52} have been used for this purpose . As shown from their dielectric functions discussed later, the former works more effectively in the longer wavelength in the mid-infrared range, whereas the latter can provide nonreciprocity for shorter wavelengths. We note that, though each material has been used individually for nonreciprocal emitter design, it is not clear whether and how these materials can be combined to achieve even broader band of nonreciprocal thermal emission. Therefore,

we choose these materials as our model nonreciprocal materials and focus on structures shown in Fig. 1(b) that have InAs layers on top of Weyl semimetal layers on a reflective substrate, where we use silver as substrate in this study. In this way, we rule out the type of structures that possess alternating InAs and Weyl semimetal layers since they can be very challenging to fabricate in practice. We will also seek to optimize the structures containing InAs only, so that we can compare with the state-of-the-art design²² and showcase the significant improvement through using our approach.

We consider transverse magnetic (TM) waves with a magnetic field along the $-z$ direction, and consider the Voigt configurations.²⁹ In this way, we trigger the nonreciprocity for the radiative properties at different polar angle θ in the x - y plane. For InAs, we apply an external magnetic field (B field) along the $-z$ direction.^{53,54} In this case, the permittivity tensor of each InAs layer reads¹⁵

$$\boldsymbol{\epsilon} = \begin{bmatrix} \epsilon_{xx} & \epsilon_{xy} & 0 \\ \epsilon_{yx} & \epsilon_{yy} & 0 \\ 0 & 0 & \epsilon_{zz} \end{bmatrix}. \quad (5)$$

The components of the permittivity tensor for InAs can be expressed as

$$\begin{aligned} \epsilon_{xx} = \epsilon_{yy} &= \epsilon_{\infty} - \frac{\omega_p^2(\omega + i\Gamma)}{\omega[(\omega + i\Gamma)^2 - \omega_c^2]}, \\ \epsilon_{xy} &= -\epsilon_{yx} = \frac{i\omega_p^2\omega_c}{\omega[(\omega + i\Gamma)^2 - \omega_c^2]}, \\ \epsilon_{zz} &= \epsilon_{\infty} - \frac{\omega_p^2}{\omega(\omega + i\Gamma)}, \end{aligned} \quad (6)$$

where ω is the angular frequency, ϵ_{∞} is the high-frequency permittivity, Γ is the damping rate, $\omega_p = \sqrt{n_e e^2 / (m^* \epsilon_0)}$ is the plasma frequency, and $\omega_c = eB / m^*$ is the cyclotron frequency. Here, n_e is the carrier concentration, e is the elementary charge, m^* is the effective electron mass, and ϵ_0 is the vacuum permittivity. We focus on the ENZ point where the real part of ϵ_{xx} crosses zero^{15,55–58} and brings a significant enhancement to $\epsilon_{xy} / \text{Re}(\epsilon_{xx})$ and the nonreciprocal

effect.²⁹ By adjusting the carrier concentration n_e , which we can experimentally control while fabricating InAs among other parameters in Eq. (6), the ENZ point shifts, allowing us to control the wavelength at which the ENZ region occurs.

The nonreciprocal effect in magnetic Weyl semimetal layers is intrinsic and does not require an external magnetic field.¹⁶ The momentum separation of the Weyl cones, $2\mathbf{b}$, acts similarly to an applied magnetic field in magneto-optical systems. We set $\mathbf{b} = -b\mathbf{k}_z$ to be also along the $-z$ direction (Fig. 1(b)) following the Voigt configuration and, in this case, the permittivity tensor of Weyl semimetal has the same format as Eq. (5).¹⁶ Similar to InAs, the nonreciprocal effect for Weyl is significantly enhanced when the diagonal element ε crosses zero at ENZ point.

The diagonal elements of the permittivity of each Weyl semimetal layer read $\varepsilon_{xx} = \varepsilon_{yy} = \varepsilon_{zz} = \varepsilon_b + \frac{i\sigma}{\omega\varepsilon_0}$, where ε_b is the background permittivity, ω is the radiation frequency, and σ is the bulk conductivity obtained from¹⁶

$$\sigma = \frac{\varepsilon_0 r_s g E_F}{6\hbar} \Omega G\left(\frac{E_F \Omega}{2}\right) + i \frac{\varepsilon_0 r_s g E_F}{6\pi\hbar} \left\{ \frac{4}{\Omega} \left[1 + \frac{\pi^2}{3} \left(\frac{k_B T}{E_F} \right)^2 \right] + 8\Omega \int_0^{\xi_c} \frac{G(E_F \xi) - G\left(\frac{E_F \Omega}{2}\right)}{\Omega^2 - 4\xi^2} \xi d\xi \right\}. \quad (7)$$

Here, $r_s = e^2/(4\pi\varepsilon_0\hbar\nu_F)$ is the effective fine structure constant, \hbar is the reduced Planck constant, and ν_F is the Fermi velocity. $\Omega = \hbar(\omega + i\tau^{-1})/E_F$ is the normalized complex frequency, τ^{-1} is the scattering rate, E_F is the Fermi level, and T is the temperature, which we assume is 300 K for this study. $G(E) = n(-E) - n(E)$, where $n(E)$ is the Fermi-Dirac distribution function, g is the number of Weyl points, and k_B is the Boltzmann constant. $\xi_c = E_C/E_F$ is the normalized cutoff energy, where E_C is the cutoff energy beyond which the band dispersion is no longer linear. In addition, the off-diagonal element of the permittivity tensor of each Weyl semimetal layer is calculated as

$$\varepsilon_{xy} = -\varepsilon_{yx} = i \frac{be^2}{2\pi^2\hbar\omega}. \quad (8)$$

By tuning the Fermi level E_F —a parameter similar to n_e for InAs that can be adjusted

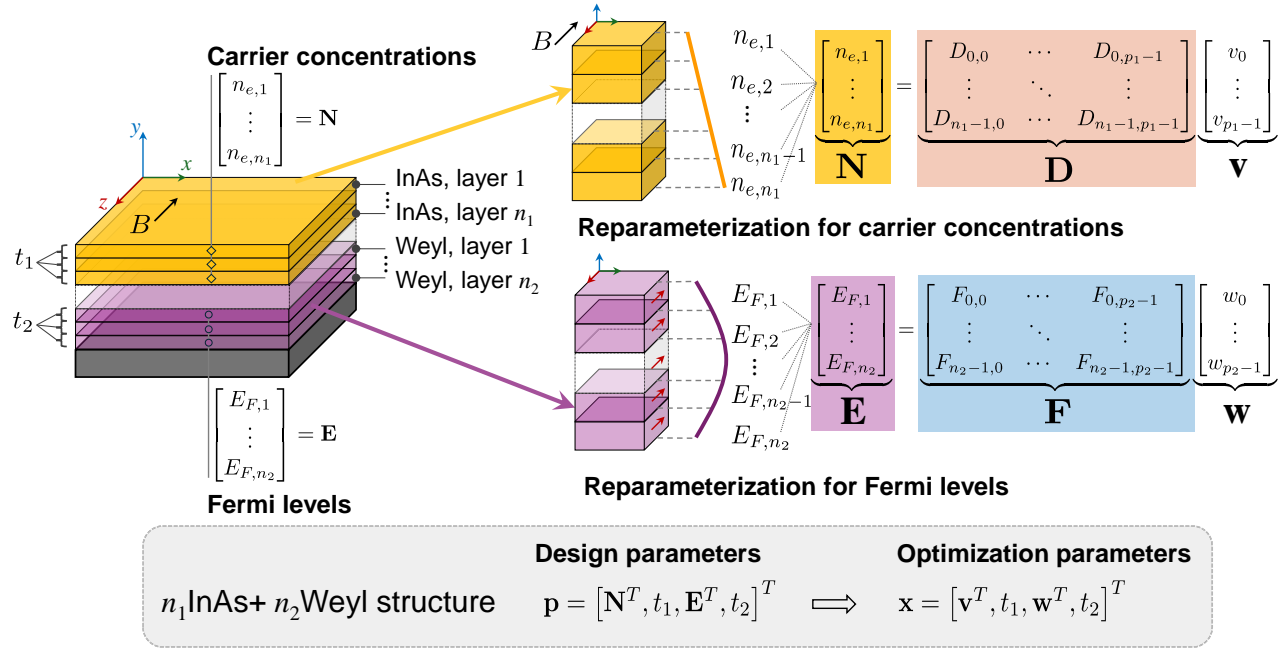


Figure 2: Design parameters \mathbf{p} for a nonreciprocal emitter of interest and their reparameterization into \mathbf{x} . The structure consists of n_1 InAs layers with carrier concentrations \mathbf{N} and thickness t_1 , and n_2 Weyl semimetal layers with Fermi levels \mathbf{E} and thickness t_2 . After reparameterizing \mathbf{N} and \mathbf{E} , the number of parameters reduces from $n_1 + n_2 + 2$ to $p_1 + p_2 + 2$, where $p_1 \leq n_1$ and $p_2 \leq n_2$ are the numbers of columns of \mathbf{D} and \mathbf{F} , respectively.

in experiments—the ENZ point of the Weyl semimetal can be modified, which shifts the wavelength at which the associated resonance occurs.

Optimization problem

For the structure shown in Fig. 1(b), each layer exhibits a distinct ENZ point, resulting in enhanced nonreciprocity across different wavelengths. Due to the multilayer design, with each layer having a unique ENZ point, broadband nonreciprocity can be achieved over a wide wavelength range. To optimize the contrast between absorptivity and emissivity across this broad bandwidth, it is necessary to solve an optimization problem to determine the optimal values of design parameters: the carrier concentrations for InAs layers, the Fermi levels for Weyl semimetal layers, and the thickness of each layer in the multilayer structure. In this study, we only try to optimize the mentioned design parameters, while assuming other

parameters of the dielectric functions of InAs and Weyl semimetals are fixed. For the InAs, the high-frequency permittivity and the effective electron mass of InAs are $\varepsilon_\infty = 12.37$ and $m^* = 0.033m_e$,⁵⁹ respectively, where m_e is the electron mass. The damping rate of InAs is set as $\Gamma = 5.9 \times 10^{12}$ rad/s.²² The background permittivity, the number of Weyl points, the Fermi velocity, the relaxation time, and the cutoff energy of Weyl semimetals are $\varepsilon_b = 6.2$, $g = 2$, $\tau = 10^{-12}$ s, $\nu_F = 0.83 \times 10^5$ m/s, and $E_C = 0.45$ eV, respectively.¹⁶

Our optimization starts by defining an objective function. Denote emitter design parameters $\mathbf{p} \in \mathbb{R}_+^p$, wavelength $\lambda \in \mathbb{R}_+$, and angle of incidence $\theta \in \mathbb{R}_+$. Let $\alpha(\mathbf{p}, \lambda, \theta)$ and $\varepsilon(\mathbf{p}, \lambda, \theta)$ be the local functions for the absorptivity and emissivity of this emitter, respectively. The local function for the contrast between the absorptivity and emissivity is defined as:

$$\eta(\mathbf{p}, \lambda, \theta) = \alpha(\mathbf{p}, \lambda, \theta) - \varepsilon(\mathbf{p}, \lambda, \theta), \quad (9)$$

where $\eta \in [-1, 1]$. Achieving maximum or minimum contrast is equivalent since the sign of the contrast can be flipped by switching the magnetic field. Figure 2 shows the design parameters \mathbf{p} for a nonreciprocal thermal emitter that is the combination of n_1 doped InAs layers on top of n_2 Weyl semimetal layers. For this structure, \mathbf{p} has n_1 distinct carrier concentrations $n_{e,i}$ ($i = 1, \dots, n_1$) for the InAs layers, the thickness t_1 of each InAs layer, n_2 distinct Fermi levels $E_{F,j}$ ($j = 1, \dots, n_2$) for the Weyl semimetal layers, and the thickness t_2 of each Weyl semimetal layer. Here we simplify the optimization problem by using the same thickness for layers of each type of material.

Maintaining the sign of the contrast, we formulate the following optimization problem for the nonreciprocal emitter, aimed at finding an optimal structure that achieves negative contrast over broad wavelength and angular ranges:

$$\underset{\mathbf{p} \in \mathcal{P}}{\text{minimize}} \quad \tilde{\eta}(\mathbf{p}), \quad (10)$$

where $\tilde{\eta}$ represents the normalized contrast, which serves as the figure of merit for the

153 broadband nonreciprocity, and $\mathcal{P} \subset \mathbb{R}_+^p$ is the feasible domain of \mathbf{p} . The normalized contrast
 154 $\tilde{\eta} \in [-1, 1]$ represents the contrast averaged across the considered ranges of wavelengths and
 155 angles. $\tilde{\eta}$ is defined as follows:

$$\tilde{\eta}(\mathbf{p}) = \frac{\int_{\lambda_L}^{\lambda_U} \int_0^{\pi/2} \eta(\mathbf{p}, \lambda, \theta) \sin \theta \cos \theta \, d\theta \, d\lambda}{\int_{\lambda_L}^{\lambda_U} \int_0^{\pi/2} \sin \theta \cos \theta \, d\theta \, d\lambda}, \quad (11)$$

156 where λ_L and λ_U are the lower and upper values of the considered wavelength range, re-
 157 spectively. A numerical quadrature method for efficiently computing the integrals in the
 158 numerator of $\tilde{\eta}(\mathbf{p})$ is given in the Supporting Information.

159 We further apply a reparameterization strategy to the objective function $\tilde{\eta}(\mathbf{p})$ to enforce
 160 desired design constraints on the emitter structure and/or other constraints on the opti-
 161 mization problem. The design constraints allow for experimental control over the profiles
 162 (e.g., linear or nonlinear) of carrier concentrations and Fermi levels inside the multilayer
 163 structures which profoundly affect the contrast value.⁶⁰ Meanwhile, the reparameterization
 164 ensures that the number of optimization parameters remains manageable for the optimizer,
 165 which is crucial when there are many design parameters.

166 The reparameterization strategy transforms $\tilde{\eta}(\mathbf{p})$ over the design parameter space $\mathbf{p} \in \mathcal{P}$
 167 into $\bar{\eta}(\mathbf{x})$ over the space of optimization parameters $\mathbf{x} = \phi(\mathbf{p}) \in \mathbb{R}^d$, with the reparameteriza-
 168 tion map $\phi(\cdot) : \mathbb{R}_+^p \mapsto \mathbb{R}^d$ encapsulating all desired constraints. As a result, the optimization
 169 problem after reparameterization reads

$$\underset{\mathbf{x} \in \mathcal{X}}{\text{minimize}} \quad \bar{\eta}(\mathbf{x}), \quad (12)$$

170 where $\mathcal{X} = \{\mathbf{x} \in \mathbb{R}^d | \phi^{-1}(\mathbf{x}) \in \mathcal{P}\}$ and $\bar{\eta}(\mathbf{x}) = \tilde{\eta}(\phi^{-1}(\mathbf{x}))$. Thus, instead of solving problem
 171 (10) directly, we solve problem (12) and recover an optimal set of \mathbf{p} from the resulting
 172 optimal set of \mathbf{x} .

173 Given a specific value of the optimization parameters \mathbf{x} and the reparameterization map
 174 $\phi(\cdot)$, computing $\bar{\eta}(\mathbf{x})$ is straightforward. We first recover the design parameter $\mathbf{p} = \phi^{-1}(\mathbf{x})$.

We then compute $\tilde{\eta}(\mathbf{p})$ and set $\bar{\eta}(\mathbf{x})$ as $\tilde{\eta}(\mathbf{p})$.

Figure 2 details the reparameterization technique used in this study. This technique transforms the carrier concentrations $\mathbf{N} = [n_{e,1}, \dots, n_{e,n_1}]^T \in \mathbb{R}^{n_1}$ for the InAs layers and Fermi levels $\mathbf{E} = [E_{F,1}, \dots, E_{F,n_2}]^T \in \mathbb{R}^{n_2}$ for the Weyl semimetal layers into optimization parameters $\mathbf{v} \in \mathbb{R}^{p_1}$ and $\mathbf{w} \in \mathbb{R}^{p_2}$, respectively, using two linear maps $\mathbf{D} \in \mathbb{R}^{n_1 \times p_1}$ and $\mathbf{F} \in \mathbb{R}^{n_2 \times p_2}$ where $p_1 \leq n_1$ and $p_2 \leq n_2$. By carefully designing the span of \mathbf{D} and \mathbf{F} , we can reduce the number of parameters for our optimization problem, which is now formulated for \mathbf{v} and \mathbf{w} . This reduction is crucial when n_1 or n_2 is large, as the performance of the optimization algorithm strongly depends on the problem’s input dimension. Bayesian optimization, for example, is most effective for problems of less than 20 dimensions.³⁸ By further designing the entries of each column of \mathbf{D} or \mathbf{F} , we are able to impose specific geometrical properties on the emitter, for example, linear profiles of carrier concentrations or quadratic profiles of Fermi levels (see Fig. 2). The detailed computations for \mathbf{D} and \mathbf{F} are provided in the Supporting Information.

Optimizer

Bayesian optimization (BO)^{34–39} is a successful approach to optimizing functions that are costly to evaluate, cannot be evaluated exactly, have no analytical expressions, or offer no efficient way to compute their derivatives.³⁹ It finds applications in diverse domains of science and engineering, including photonic curing processes,⁶¹ adaptive experimental design,^{62,63} accelerator physics,⁶⁴ and material design,^{65–67} to name a few. BO also enables the integration of physical and mathematical insights into the optimization process.^{68–70}

In this study, we use BO to solve problem (12). This is justified because the objective function $\bar{\eta}(\mathbf{x})$ lacks a useful analytical expression and is computationally expensive. In the following, we provide an overview of BO and explain how it can be used to incrementally improve the broadband nonreciprocity of nonreciprocal emitters starting from ineffective

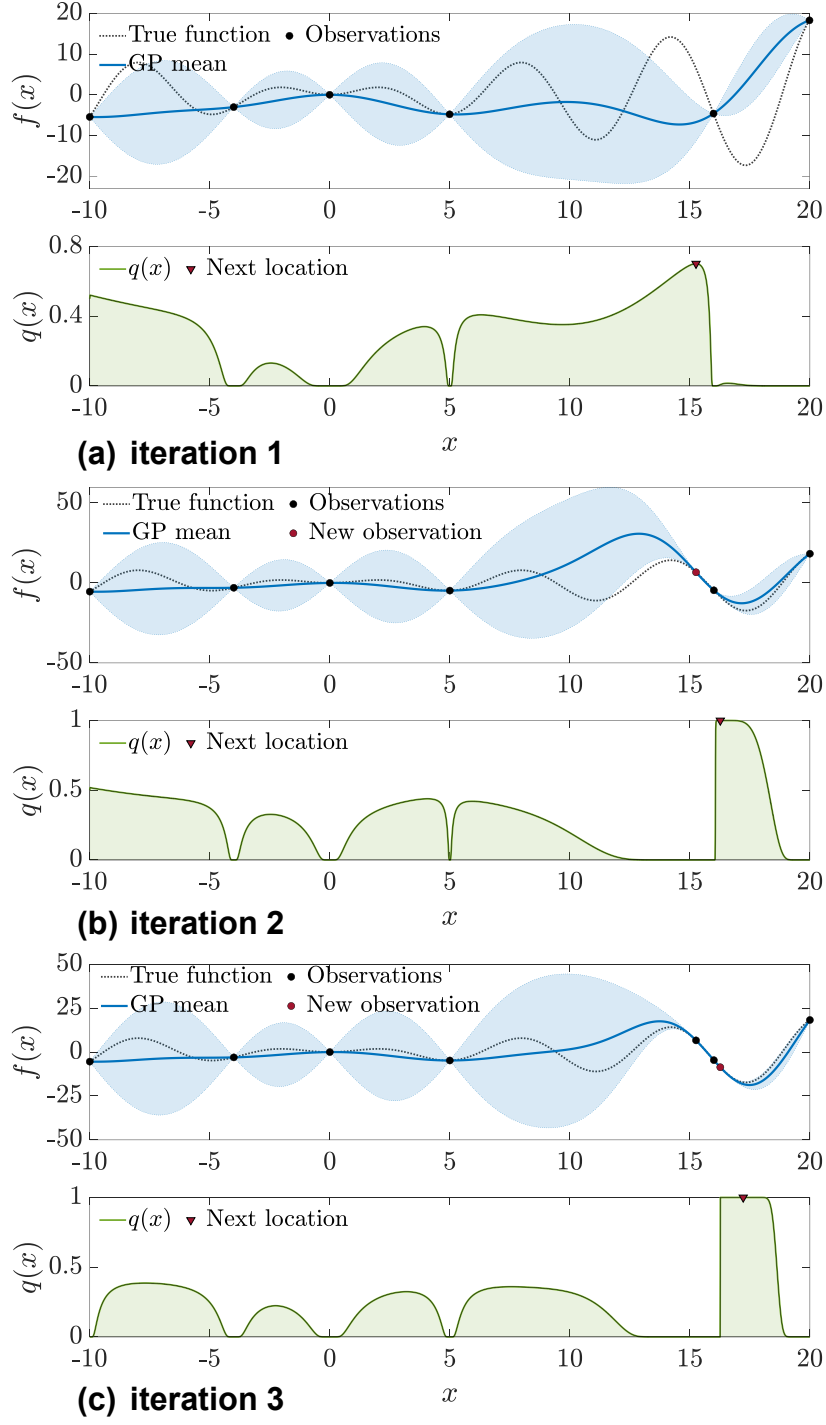


Figure 3: Schematic illustration of three consecutive iterations of BO for optimizing a univariate function $f(x)$. In each iteration, BO constructs a probabilistic model for the objective function $f(x)$ using the current data, formulates an acquisition function $q(x)$ from the model, and maximizes $q(x)$ to identify a new location to query the objective function.

ones.

Given a few observations for a specific optimization problem, BO solves the problem by repeatedly (1) constructing a probabilistic model for the objective function to represent our prior knowledge and the observations, (2) formulating an acquisition function to define what we value in the current dataset given the probabilistic model, and (3) maximizing the acquisition function to guide the optimization process. This iterative process typically terminates as it reaches a prespecified number of observations we can afford, which reflects our computational budget. Figure 3 illustrates three consecutive iterations of BO for minimizing a univariate objective function $f(x)$. BO starts with six observations of $f(x)$ and locates the true global minimizer of $f(x)$ after only three iterations (lower plot of Fig. 3c).

A Gaussian process (GP)⁷¹ model often serves as the probabilistic model for BO due to its tractability and flexibility. Typically, the GP prior is specified simply by a zero mean function and a covariance function with a closed form and a few hyperparameters. Given a dataset of the objective function observations, the GP posterior can be derived by conditioning the GP prior on the dataset. This GP posterior then serves as the probabilistic model that represents our beliefs about the structure of the costly objective function. The reader is referred to the Supporting Information for the mathematical foundation of GP and the analytical formula of the GP posterior.

Once the GP posterior model has been constructed, we formulate an acquisition function to define an optimization policy representing what we wish to exploit from this model. The acquisition function maps each point in the design variable space to a score on its ability to benefit the optimization process, considering our imperfect knowledge of the objective function.^{34,72} By maximizing this acquisition function, we thus maximize the potential to obtain a better new design. We do so numerically by using, for example, a global optimization algorithm, and the resulting solution is used in the next iteration of BO for a new evaluation of the objective function. Maximizing the acquisition function is typically simpler and less computationally expensive than optimizing the costly objective function directly.

Algorithm 1 Bayesian optimization with noiseless observations

```
1: input: domain  $\mathcal{P}$  of design parameters  $\mathbf{p}$ , number of initial observations  $N$ , threshold  
   for the number of BO iterations  $K$ , reparameterization map  $\phi(\cdot)$   
2: Generate  $N$  initial observations of optimization parameters  $\mathbf{x}$   
3: for  $i = 1 : N$  do ▷ Generate initial observations of the normalized contrast  
4:    $y_i \leftarrow \bar{\eta}(\mathbf{x}_i)$   
5: end for  
6:  $\mathcal{D}_0 \leftarrow \{\mathbf{x}_i, y_i\}_{i=1}^N$  ▷ Dataset of initial observations  
7:  $\{\mathbf{x}_{\min}, y_{\min}\} \leftarrow \min\{y_i, i = 1, \dots, N\}$  ▷ The best observation found so far  
8: for  $i = N + 1 : N + K$  do  
9:    $k \leftarrow i - N$   
10:  Build a GP posterior  $\hat{\eta}_k(\mathbf{x})|\mathcal{D}_{k-1}$   
11:  Formulate an acquisition function  $q(\mathbf{x}|\mathcal{D}_{k-1})$  from  $\hat{\eta}_k(\mathbf{x})|\mathcal{D}_{k-1}$   
12:   $\mathbf{x}_k \leftarrow \arg \max_{\mathbf{x}} q(\mathbf{x}|\mathcal{D}_{k-1})$  s.t.  $\phi^{-1}(\mathbf{x}) \in \mathcal{P}; \mathbf{x} \notin \mathcal{D}_{k-1}$  ▷ Maximize the acquisition  
   function  
13:   $y_k \leftarrow \bar{\eta}(\mathbf{x}_k)$  ▷ Obtain a new observation of the normalized contrast  
14:   $\mathcal{D}_k \leftarrow \mathcal{D}_{k-1} \cup \{\mathbf{x}_k, y_k\}$  ▷ Update the dataset of observations  
15:   $\{\mathbf{x}_{\min}, y_{\min}\} \leftarrow \min\{y_{\min}, y_k\}$  ▷ The best observation found so far  
16: end for  
17: return  $\{\mathbf{x}_{\min}, y_{\min}\}$  and  $\mathbf{p}_{\min} \leftarrow \phi(\mathbf{x}_{\min})$ 
```

227 In Algorithm 1, we outline the use of BO for optimizing a nonreciprocal thermal emitter
228 of interest. We begin with specifying the design parameter domain \mathcal{P} , the number N of
229 initial observations of the normalized contrast $\bar{\eta}(\mathbf{x})$, and the threshold K for the number of
230 BO iterations, followed by defining the reparameterization map $\phi(\cdot)$ (Line 1). To construct
231 an initial dataset \mathcal{D}_0 (Line 6), which is necessary for initializing BO, we randomly generate
232 a set of N samples for the optimization parameters \mathbf{x} using Latin hypercube sampling⁷³
233 (Line 2), and subsequently evaluate $\bar{\eta}(\mathbf{x})$ at the generated samples using rigorous coupled-
234 wave analyses^{74,75} (Line 4). Here, we assume that the evaluated values of $\bar{\eta}(\mathbf{x})$ are noiseless,
235 which means the numerical results perfectly capture the distribution of nonreciprocal thermal
236 radiation in the emitter without introducing any numerical errors.

237 The for-loop of BO (Line 8 to Line 16) commences with constructing a GP posterior
238 $\hat{\eta}_k(\mathbf{x})$ for $\bar{\eta}(\mathbf{x})$ from the current dataset \mathcal{D}_{k-1} (Line 10), where $k = 1, \dots, K$ represents
239 the index variable for the loop. It then formulates an acquisition function $q(\mathbf{x})$ based on
240 $\hat{\eta}_k(\mathbf{x})$ (Line 11) and maximizes $q(\mathbf{x})$ for a new observation \mathbf{x}_k of the optimization parameters

(Line 12). To avoid reselecting points already seen in the current dataset \mathcal{D}_{k-1} , the constraint $\mathbf{x} \notin \mathcal{D}_{k-1}$ is imposed to the maximization of $q(\mathbf{x})$ (Line 12). Finally, the algorithm evaluates the normalized contrast $y_k = \bar{\eta}(\mathbf{x}_k)$ at the new point \mathbf{x}_k , and updates the dataset with \mathbf{x}_k and y_k for use in the next iteration (Lines 13 and 14). The final optimal solution is the best observation found among points of the dataset recommended by the algorithm (Lines 15 and 17).

Results and discussion

We present the optimization results for two multilayer structures of nonreciprocal thermal emitters: a 3-layer InAs structure and a 6-layer 3InAs+3Weyl structure (i.e., three layers of InAs on top of three layers of Weyl semimetal). By considering these structures, we aim to investigate how a combination of InAs and Weyl semimetal can improve broadband nonreciprocity. For this purpose, we also optimize other two structures, namely a 5-layer InAs structure and an 8-layer 5InAs+3Weyl structure. The optimization results for these structures are provided in the Supporting Information. To evaluate the performance of the obtained optimal structures, we compare the contrast between absorptivity and emissivity of them with that of the state-of-the-art 10-layer InAs structure proposed by Liu et al.²²

Initialization

We consider wavelengths λ ranging from 5 to 40 μm , which covers the thermal infrared range and is much broader than that in existing works. We analyze TM waves under an applied magnetic field of $B = 1.5$ T. The reparameterization is carefully designed for each structure to ensure that the carrier concentrations of InAs and the Weyl Fermi levels across the layers conform to a polynomial of up to second order. As a result, there are four optimization parameters for 3-layer and 5-layer InAs structures, and eight parameters for 6-layer 3InAs+3Weyl and 8-layer 5InAs+3Weyl structures. For 5-layer InAs and 8-layer

5InAs+3Weyl structures, the number of optimization parameters is less than the number of design parameters. Further details on the reparameterization scheme are provided in the Supporting Information.

There are several settings for BO and the optimizer used for maximizing the acquisition function at each BO iteration. The GP prior is determined by a zero-mean function and the squared exponential covariance function (see Eq. (S2) of the Supporting Information). The carrier concentrations of InAs layers, the Fermi levels of Weyl semimetal layers, and the layer thicknesses are selected such that $n_{e,i} \in [1, 10] \times 10^{17}$ atoms/cm³, $E_{F,j} \in [10^{-3}, 0.5]$ eV, and $t_1, t_2 \in [100, 5000]$ nm. The number of initial observations of the normalized contrast is $N = 5d$, where d is the number of optimization parameters \mathbf{x} . The threshold for the number of BO iterations is set as $K = 150$ for 3-layer InAs structure, and $K = 1000$ for 6-layer 3InAs+3Weyl structure. BO formulates two canonical improvement-based acquisition functions: lower confidence bound (LCB) and probability of improvement (PI). Their analytical formulas are provided in the Supporting Information. To maximize each of these acquisition functions, BO uses a multi-start local optimization algorithm with 500 random starting points over the space of \mathbf{x} . The tolerance for the first-order optimality measure and the upper bound on the magnitude of any constraint functions are set at 10^{-16} . BO is implemented in MATLAB and executed on the Carya Cluster at the University of Houston.

Optimized 3-layer InAs structure

Figure 4 show the optimization results for the 3-layer InAs structure obtained from five different BO trials of LCB and five different trials of PI, with each set of trials utilizing distinct initial datasets. Despite starting from different initial values, all BO trials converge to a unique normalized contrast value of $\bar{\eta} = -16.9\%$ after 100 iterations (i.e., 20 + 100 objective function calls) for LCB and 125 iterations (i.e., 20 + 125 objective function calls) for PI, see Fig. 4(a). Figure 4(b) compares the contrast values of 3-layer InAs structures associated with the first and last iterations of the first BO trial of LCB with that from

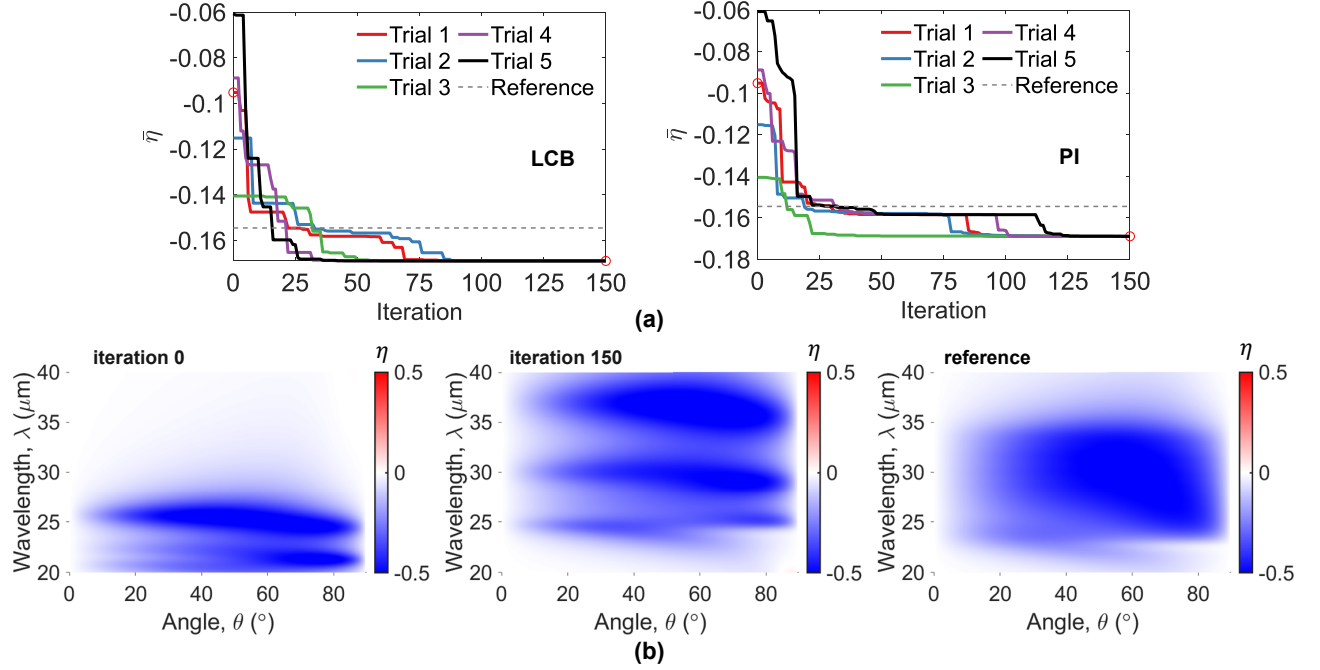


Figure 4: Optimization results for 3-layer InAs structure in comparison with the state-of-the-art 10-layer InAs structure (reference).²² (a) Optimization histories from LCB and PI. (b) Comparison of contrast values of the initial and final structures from the first and last iterations of the first LCB trial, and the state-of-the-art 10-layer InAs structure.

the state-of-the-art 10-layer InAs structure. We see that, although BO starts from a less effective initial structure (left panel), it can provide an optimal structure (middle panel) with negative contrast better than that of the state-of-the-art structure (right panel) with $\bar{\eta} = -15.4\%$, confirming its crucial role in enhancing the nonreciprocity of the 3-layer InAs structure. Moreover, it shows we can achieve substantial nonreciprocal effects with only a few layers.

Table 1 lists the optimal parameters for the best 3-layer InAs structures obtained from LCB and PI. The optimal structures from these acquisition functions are almost identical. Notably, the carrier concentrations of these optimal structures exhibit a linear increase from the top to the bottom layers.

Figure 5 shows the absorptivity and emissivity over the considered range of incidence angles for the 3-layer InAs structures from the first and last iterations of the first BO trial using LCB, as well as those of the state-of-the-art structure. We see that BO enhances the

Table 1: Carrier concentrations of InAs and layer thickness for the best 3-layer InAs structures from LCB and PI.

Parameter	LCB	PI
$n_{e,1}$ ($\times 10^{17}$ atoms/cm ³)	3.353	3.367
$n_{e,2}$ ($\times 10^{17}$ atoms/cm ³)	5.212	5.181
$n_{e,3}$ ($\times 10^{17}$ atoms/cm ³)	7.353	7.367
t_1 (nm)	1243	1247

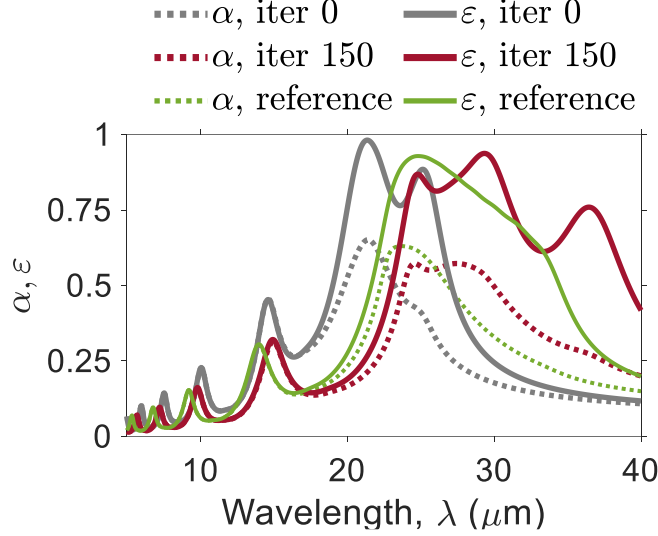


Figure 5: Absorptivity (α) and emissivity (ε) of the initial and final 3-layer InAs structures from the first and last iterations of the first LCB trial, and the state-of-the-art 10-layer InAs structure (reference).²²

nonreciprocity of the 3-layer InAs structure by increasing the absorptivity at wavelength values from 25 to 40 μm , which correspond to the upper region of the considered spectrum.

Optimized 6-layer 3InAs+3Weyl structure

Figure 6 presents the optimization results for the 6-layer 3InAs+3Weyl structure. Although different BO trials for this structure using LCB and PI do not converge to a single contrast value after 1000 iterations, they demonstrate significant improvements in the nonreciprocity. The best structures recommended by LCB and PI achieve the same negative contrast value of $\bar{\eta} = -24.4\%$, which is notably superior to that of the optimal 3-layer InAs structure with $\bar{\eta} = -16.9\%$ and that of the state-of-the-art 10-layer InAs structure with $\bar{\eta} = -15.4\%$.

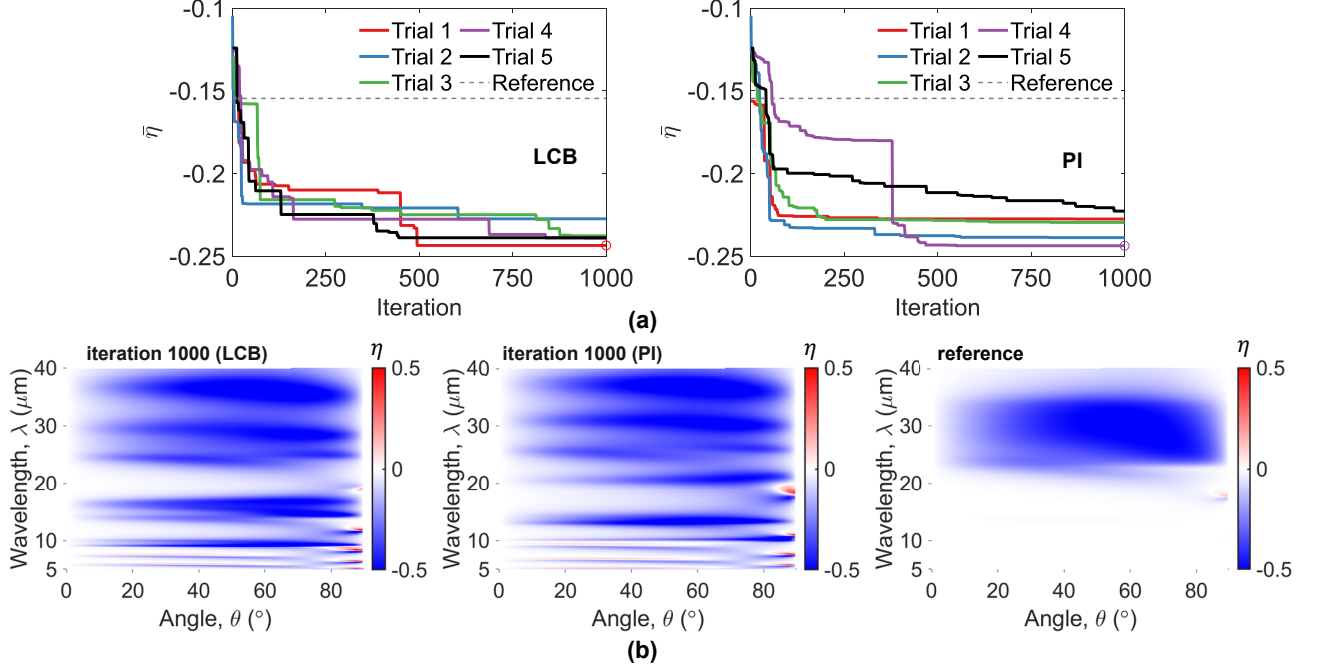


Figure 6: Optimization results for 6-layer 3InAs+3Weyl structure in comparison with the state-of-the-art 10-layer InAs structure (reference).²² (a) Optimization histories from LCB and PI. (b) Comparison of contrast values of the best structures from LCB and PI, and the state-of-the-art 10-layer InAs structure.

As shown in Fig. 6(b) and Fig. 7, the use of three InAs layers atop three Weyl semimetal layers enhances the nonreciprocity at wavelengths in both the lower and upper regions of the considered spectrum. Specifically, the top InAs layers improve the absorptivity at wavelength values from 25 to 40 μm , while the bottom Weyl semimetal layers focus on improving the absorptivity at wavelengths from 5 to 15 μm .

Table 2 lists the optimal parameters for the best 6-layer 3InAs+3Weyl structures obtained from LCB and PI. While the two acquisition functions yield the same optimal contrast value ($\bar{\eta} = -24.4\%$), they provide two different sets of optimal parameters. Nevertheless, the carrier concentrations of the InAs layers of these optimal structures still increase linearly from the top to the bottom. Additionally, the thickness of the Weyl semimetal layers reaches the lower bound of its defined domain, indicating that further improvement may be possible with even thinner layers.

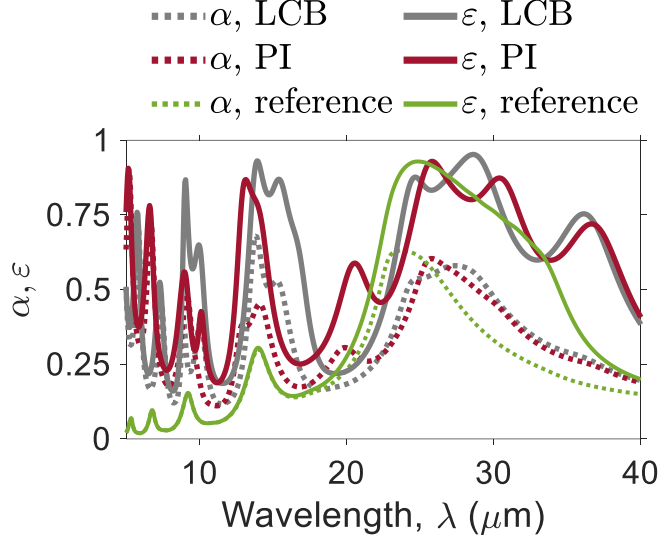


Figure 7: Absorptivity (α) and emissivity (ε) of the best 6-layer 3InAs+3Weyl structures from LCB and PI, and the state-of-the-art 10-layer InAs structure (reference).²²

Table 2: Carrier concentrations of InAs, Weyl Fermi levels, and layer thicknesses for the best 6-layer 3InAs+3Weyl structures from LCB and PI.

Parameter	LCB	PI
$n_{e,1}$ ($\times 10^{17}$ atoms/cm ³)	3.416	3.308
$n_{e,2}$ ($\times 10^{17}$ atoms/cm ³)	5.454	4.861
$n_{e,3}$ ($\times 10^{17}$ atoms/cm ³)	7.416	6.777
t_1 (nm)	1203	1066
$E_{F,1}$ (eV)	0.097	0.061
$E_{F,2}$ (eV)	0.148	0.103
$E_{F,3}$ (eV)	0.097	0.132
t_2 (nm)	100	100

Conclusion

We present an optimization approach combining BO and reparameterization that demonstrates optimal broadband nonreciprocal thermal emitter performance, surpassing state-of-the-art broadband nonreciprocal effects in the infrared range of thermal radiation using doped InAs and Weyl semimetal materials. Starting from a less effective structure, the proposed approach incrementally improves the broadband nonreciprocity of the structure by repeatedly reparameterizing the normalized contrast, constructing a probabilistic surrogate model for the reparameterized contrast, maximizing a cheap-to-compute acquisition function

formulated from the constructed surrogate model to identify a promising new structure, and updating the surrogate model with the new structure. The optimal structure is the best structure among those recommended by the optimization algorithm upon its termination. Optimization results indicate that our approach can propose an optimal structure of only three InAs layers that outperforms the current state-of-the-art 10-layer InAs structure.²² Additionally, the broadband nonreciprocal effect considerably increases when using InAs and Weyl semimetals, which shows the feasibility of combining different nonreciprocal materials for enhanced nonreciprocity. The significant improvements in the designed emitters highlight the role of numerical optimization in advancing practical nonreciprocal thermal emitter development. Our approach can also be adapted to optimize more general structures containing patterns. In an ongoing study, we conduct experiments to validate the performance of the optimized structures. We then combine the experimental and numerical observations within the framework of multi-fidelity BO^{69,70,76–78} to further enhance our design approach.

Acknowledgement

The authors acknowledge the funding from the University of Houston through the SEED program and the National Science Foundation under Grant No. CBET-2314210, and the support of the Research Computing Data Core at the University of Houston for assistance with the calculations carried out in this work.

Associated content

Data availability statement The data underlying this study are not publicly available as they form part of an ongoing study. The code for Bayesian optimization is available from the corresponding author upon reasonable request.

Supporting information

The mathematical foundation of Gaussian process models, the expressions of LCB and PI acquisition functions, the quadrature method for computing the contrast between absorptivity and emissivity at a particular value of design parameters, the details of the reparameterization scheme, and additional results for 5-layer InAs and 8-layer 5InAs+3Weyl structures.

References

- (1) Greffet, J.-J.; Carminati, R.; Joulain, K.; Mulet, J.-P.; Mainguy, S.; Chen, Y. Coherent emission of light by thermal sources. *Nature* **2002**, *416*, 61–64.
- (2) Fan, S. Thermal photonics and energy applications. *Joule* **2017**, *1*, 264–273.
- (3) Baranov, D. G.; Xiao, Y.; Nechepurenko, I. A.; Krasnok, A.; Alù, A.; Kats, M. A. Nanophotonic engineering of far-field thermal emitters. *Nature Materials* **2019**, *18*, 920–930.
- (4) Li, Y.; Li, W.; Han, T.; Zheng, X.; Li, J.; Li, B.; Fan, S.; Qiu, C.-W. Transforming heat transfer with thermal metamaterials and devices. *Nature Reviews Materials* **2021**, *6*, 488–507.
- (5) Kirchhoff, G. In *Von Kirchhoff bis Planck: Theorie der Wärmestrahlung in historisch-kritischer Darstellung*; Schöpf, H.-G., Ed.; Vieweg+Teubner Verlag, 1978; pp 131–151.
- (6) Planck, M. *The Theory of Heat Radiation*; Blakiston, 1914.
- (7) Ries, H. Complete and reversible absorption of radiation. *Applied Physics B* **1983**, *32*, 153–156.
- (8) Snyder, W. C.; Wan, Z.; Li, X. Thermodynamic constraints on reflectance reciprocity and Kirchhoff’s law. *Applied Optics* **1998**, *37*, 3464–3470.
- (9) Green, M. A. Time-asymmetric photovoltaics. *Nano Letters* **2012**, *12*, 5985–5988.
- (10) Buddhiraju, S.; Santhanam, P.; Fan, S. Thermodynamic limits of energy harvesting from outgoing thermal radiation. *Proceedings of the National Academy of Sciences* **2018**, *115*, E3609–E3615.

- (11) Li, W.; Buddhiraju, S.; Fan, S. Thermodynamic limits for simultaneous energy harvesting from the hot sun and cold outer space. *Light: Science & Applications* **2020**, *9*, 68.
- (12) Park, Y.; Zhao, B.; Fan, S. Reaching the ultimate efficiency of solar energy harvesting with a nonreciprocal multijunction solar cell. *Nano Letters* **2021**, *22*, 448–452.
- (13) Jafari Ghalekohneh, S.; Zhao, B. Nonreciprocal solar thermophotovoltaics. *Physical Review Applied* **2022**, *18*, 034083.
- (14) Park, Y.; Omair, Z.; Fan, S. Nonreciprocal thermophotovoltaic systems. *ACS Photonics* **2022**, *9*, 3943–3949.
- (15) Zhu, L.; Fan, S. Near-complete violation of detailed balance in thermal radiation. *Physical Review B* **2014**, *90*, 220301.
- (16) Zhao, B.; Guo, C.; Garcia, C. A. C.; Narang, P.; Fan, S. Axion-field-enabled nonreciprocal thermal radiation in Weyl semimetals. *Nano Letters* **2020**, *20*, 1923–1927.
- (17) Shayegan, K. J.; Biswas, S.; Zhao, B.; Fan, S.; Atwater, H. A. Direct observation of the violation of Kirchhoff’s law of thermal radiation. *Nature Photonics* **2023**, *17*, 891–896.
- (18) Park, Y.; Zhao, B.; Fan, S. Reaching the ultimate efficiency of solar energy harvesting with a nonreciprocal multijunction solar cell. *Nano Letters* **2022**, *22*, 448–452.
- (19) Zhang, Z.; Zhu, L. Nonreciprocal thermal photonics for energy conversion and radiative heat transfer. *Physical Review Applied* **2022**, *18*, 027001.
- (20) Yang, S.; Liu, M.; Zhao, C.; Fan, S.; Qiu, C.-W. Nonreciprocal thermal photonics. *Nature Photonics* **2024**, *18*, 412–424.
- (21) Zhu, L.; Fan, S. Persistent directional current at equilibrium in nonreciprocal many-body near field electromagnetic heat transfer. *Physical Review Letters* **2016**, *117*, 134303.

- (22) Liu, M.; Xia, S.; Wan, W.; Qin, J.; Li, H.; Zhao, C.; Bi, L.; Qiu, C.-W. Broadband mid-infrared non-reciprocal absorption using magnetized gradient epsilon-near-zero thin films. *Nature Materials* **2023**, *22*, 1196–1202.
- (23) Dong, J.; Zhang, W.; Liu, L. Nonreciprocal thermal radiation of nanoparticles via spin-directional coupling with reciprocal surface modes. *Applied Physics Letters* **2021**, *119*, 021104.
- (24) Fan, L.; Guo, Y.; Papadakis, G. T.; Zhao, B.; Zhao, Z.; Buddhiraju, S.; Orenstein, M.; Fan, S. Nonreciprocal radiative heat transfer between two planar bodies. *Physical Review B* **2020**, *101*, 085407.
- (25) Khandekar, C.; Buddhiraju, S.; Wilkinson, P. R.; Gimzewski, J. K.; Rodriguez, A. W.; Chase, C.; Fan, S. Nonequilibrium lateral force and torque by thermally excited non-reciprocal surface electromagnetic waves. *Physical Review B* **2021**, *104*, 245433.
- (26) Gelbwaser-Klimovsky, D.; Graham, N.; Kardar, M.; Krüger, M. Near field propulsion forces from nonreciprocal media. *Physical Review Letters* **2021**, *126*, 170401.
- (27) Shi, Y.; Li, W.; Raman, A.; Fan, S. Optimization of multilayer optical films with a memetic algorithm and mixed integer programming. *ACS Photonics* **2018**, *5*, 684–691.
- (28) Yu, S.; Zhou, P.; Xi, W.; Chen, Z.; Deng, Y.; Luo, X.; Li, W.; Shiomi, J.; Hu, R. General deep learning framework for emissivity engineering. *Light: Science & Applications* **2023**, *12*, 291.
- (29) Zhao, B.; Shi, Y.; Wang, J.; Zhao, Z.; Zhao, N.; Fan, S. Near-complete violation of Kirchhoff’s law of thermal radiation with a 0.3 T magnetic field. *Optics Letters* **2019**, *44*, 4203–4206.
- (30) Zhang, Z.; Zhu, L. Broadband nonreciprocal thermal emission. *Physical Review Applied* **2023**, *19*, 014013.

- (31) Wang, L.; García de Abajo, F. J.; Papadakis, G. T. Maximal violation of Kirchhoff’s law in planar heterostructures. *Physical Review Research* **2023**, *5*, L022051.
- (32) Jafari Ghalekohneh, S.; Du, C.; Zhao, B. Controlling the contrast between absorptivity and emissivity in nonreciprocal thermal emitters. *Applied Physics Letters* **2024**, *124*, 101104.
- (33) Zhu, L.; Fan, S. Persistent directional current at equilibrium in nonreciprocal many-body near field electromagnetic heat transfer. *Physical review letters* **2016**, *117*, 134303.
- (34) Jones, D. R.; Schonlau, M.; Welch, W. J. Efficient global optimization of expensive black-box functions. *Journal of Global Optimization* **1998**, *13*, 455–492.
- (35) Brochu, E.; Cora, V. M.; de Freitas, N. A tutorial on Bayesian optimization of expensive cost functions, with application to active user modeling and hierarchical reinforcement learning. arXiv preprint arXiv:1012.2599, 2010.
- (36) Shahriari, B.; Swersky, K.; Wang, Z.; Adams, R. P.; de Freitas, N. Taking the human out of the loop: A review of Bayesian optimization. *Proceedings of the IEEE* **2016**, *104*, 148–175.
- (37) Snoek, J.; Larochelle, H.; Adams, R. P. Practical Bayesian optimization of machine learning algorithms. *Advances in Neural Information Processing Systems*. 2012; pp 2951–2959.
- (38) Frazier, P. I. In *Recent Advances in Optimization and Modeling of Contemporary Problems*; Gel, E., Ntamo, L., Eds.; INFORMS TutORials in Operations Research; INFORMS, 2018; Chapter Bayesian optimization, pp 255–278.
- (39) Garnett, R. *Bayesian optimization*; Cambridge University Press: Cambridge, UK, 2023.
- (40) Gold, H.; Pajovic, S.; Mukherjee, A.; Boriskina, S. V. GAGA for nonreciprocal emitters:

- genetic algorithm gradient ascent optimization of compact magnetophotonic crystals. *Nanophotonics* **2024**, *13*, 773–792.
- (41) Hughes, T. W.; Minkov, M.; Williamson, I. A. D.; Fan, S. Adjoint method and inverse design for nonlinear nanophotonic devices. *ACS Photonics* **2018**, *5*, 4781–4787.
 - (42) Kudyshev, Z. A.; Kildishev, A. V.; Shalaev, V. M.; Boltasseva, A. Machine learning–assisted global optimization of photonic devices. *Nanophotonics* **2021**, *10*, 371–383.
 - (43) Zhu, L.; Fan, S. Near-complete violation of detailed balance in thermal radiation. *Physical Review B* **2014**, *90*, 220301.
 - (44) Zhao, B.; Wang, J.; Zhao, Z.; Guo, C.; Yu, Z.; Fan, S. Nonreciprocal thermal emitters using metasurfaces with multiple diffraction channels. *Physical Review Applied* **2021**, *16*, 064001.
 - (45) Zhao, Z.; Guo, C.; Fan, S. Connection of temporal coupled-mode-theory formalisms for a resonant optical system and its time-reversal conjugate. *Physical Review A* **2019**, *99*, 033839.
 - (46) Zhang, Z. M.; Zhang, Z. M.; Luby *Nano/microscale heat transfer*; Springer, 2007; Vol. 410.
 - (47) Ghanekar, A.; Wang, J.; Fan, S.; Povinelli, M. L. Violation of Kirchhoff’s law of thermal radiation with space–time modulated grating. *ACS Photonics* **2022**, *9*, 1157–1164.
 - (48) Ghanekar, A.; Wang, J.; Guo, C.; Fan, S.; Povinelli, M. L. Nonreciprocal thermal emission using spatiotemporal modulation of graphene. *ACS Photonics* **2022**, *10*, 170–178.
 - (49) Shayegan, K. J.; Hwang, J. S.; Zhao, B.; Raman, A. P.; Atwater, H. A. Broadband nonreciprocal thermal emissivity and absorptivity. *Light: Science & Applications* **2024**, *13*, 176.

- (50) Pajovic, S.; Tsurimaki, Y.; Qian, X.; Chen, G. Intrinsic nonreciprocal reflection and violation of Kirchhoff’s law of radiation in planar type-I magnetic Weyl semimetal surfaces. *Physical Review B* **2020**, *102*, 165417.
- (51) Park, Y.; Asadchy, V. S.; Zhao, B.; Guo, C.; Wang, J.; Fan, S. Violating Kirchhoff’s law of thermal radiation in semitransparent structures. *ACS Photonics* **2021**, *8*, 2417–2424.
- (52) Picardi, M. F.; Moerbeek, V. I.; Pascale, M.; Papadakis, G. T. Nonreciprocity in transmission mode with planar structures for arbitrarily polarized light. *Optical Materials Express* **2024**, *14*, 2201–2209.
- (53) Pershan, P. S. Magneto-optical effects. *Journal of Applied Physics* **1967**, *38*, 1482–1490.
- (54) Aers, G. C.; Boardman, A. D. The theory of semiconductor magnetoplasmon-polariton surface modes: Voigt geometry. *Journal of Physics C: Solid State Physics* **1978**, *11*, 945.
- (55) Halterman, K.; Alidoust, M.; Zyuzin, A. Epsilon-near-zero response and tunable perfect absorption in Weyl semimetals. *Physical Review B* **2018**, *98*, 085109.
- (56) Campione, S.; Brener, I.; Marquier, F. Theory of epsilon-near-zero modes in ultrathin films. *Physical Review B* **2015**, *91*, 121408.
- (57) Kinsey, N.; DeVault, C.; Boltasseva, A.; Shalaev, V. M. Near-zero-index materials for photonics. *Nature Reviews Materials* **2019**, *4*, 742–760.
- (58) Xu, J.; Mandal, J.; Raman, A. P. Broadband directional control of thermal emission. *Science* **2021**, *372*, 393–397.
- (59) Madelung, O. *Semiconductors: data handbook*; Springer Science & Business Media, 2004.

- (60) Du, C.; Zhao, B. Controlling the ENZ profile for broadband nonreciprocal thermal emitters with high contrast between emissivity and absorptivity. Proceedings of the 10th International Symposium on Radiative Transfer. 2023.
- (61) Xu, W.; Liu, Z.; Piper, R. T.; Hsu, J. W. Bayesian optimization of photonic curing process for flexible perovskite photovoltaic devices. *Solar Energy Materials and Solar Cells* **2023**, *249*, 112055.
- (62) Talapatra, A.; Boluki, S.; Duong, T.; Qian, X.; Dougherty, E.; Arróyave, R. Autonomous efficient experiment design for materials discovery with Bayesian model averaging. *Phys. Rev. Mater.* **2018**, *2*, 113803.
- (63) Greenhill, S.; Rana, S.; Gupta, S.; Vellanki, P.; Venkatesh, S. Bayesian optimization for adaptive experimental design: A review. *IEEE Access* **2020**, *8*, 13937–13948.
- (64) Roussel, R. et al. Bayesian optimization algorithms for accelerator physics. *Physical Review Accelerators and Beams* **2024**, *27*, 084801.
- (65) Frazier, P. I.; Wang, J. In *Information Science for Materials Discovery and Design*; Lookman, T., Alexander, F. J., Rajan, K., Eds.; Springer International Publishing, 2016; Chapter Bayesian optimization for materials design, pp 45–75.
- (66) Vangelatos, Z.; Sheikh, H. M.; Marcus, P. S.; Grigoropoulos, C. P.; Lopez, V. Z.; Flamourakis, G.; Farsari, M. Strength through defects: A novel Bayesian approach for the optimization of architected materials. *Science Advances* **2021**, *7*, eabk2218.
- (67) Khatamsaz, D.; Neuberger, R.; Roy, A. M.; Zadeh, S. H.; Otis, R.; Arróyave, R. A physics informed Bayesian optimization approach for material design: application to NiTi shape memory alloys. *npj Computational Materials* **2023**, *9*, 221.
- (68) Astudillo, R.; Frazier, P. I. Thinking inside the box: a tutorial on grey-box Bayesian optimization. Proceedings of the Winter Simulation Conference. 2022; pp 1–15.

- (69) Do, B.; Zhang, R. Multi-fidelity Bayesian optimization in engineering design. arXiv preprint arXiv:2311.13050, 2023.
- (70) Zhang, R.; Alemazkoo, N. Multi-fidelity machine learning for uncertainty quantification and optimization. *Journal of Machine Learning for Modeling and Computing* **2024**, *5*.
- (71) Rasmussen, C. E.; Williams, C. K. I. *Gaussian processes for machine learning*; The MIT Press: Massachusetts, USA, 2006.
- (72) Jones, D. R. A taxonomy of global optimization methods based on response surfaces. *Journal of Global Optimization* **2001**, *21*, 345–383.
- (73) Owen, A. B. A central limit theorem for Latin hypercube sampling. *Journal of the Royal Statistical Society: Series B (Methodological)* **1992**, *54*, 541–551.
- (74) Moharam, M. G.; Gaylord, T. K. Rigorous coupled-wave analysis of planar-grating diffraction. *Journal of the Optical Society of America* **1981**, *71*, 811–818.
- (75) Yang, C.; Zhao, B.; Cai, W.; Zhang, Z. M. Mid-infrared broadband circular polarizer based on Weyl semimetals. *Optics Express* **2022**, *30*, 3035–3046.
- (76) Huang, D.; Allen, T. T.; Notz, W. I.; Miller, R. A. Sequential Kriging optimization using multiple-fidelity evaluations. *Structural and Multidisciplinary Optimization* **2006**, *32*, 369–382.
- (77) Forrester, A. I. J.; Sóbester, A.; Keane, A. J. Multi-fidelity optimization via surrogate modelling. *Proceedings of the Royal Society A: Mathematical, Physical and Engineering Sciences* **2007**, *463*, 3251–3269.
- (78) Kandasamy, K.; Dasarathy, G.; Schneider, J.; Póczos, B. Multi-fidelity Bayesian optimisation with continuous approximations. Proceedings of the 34th International Conference on Machine Learning. 2017; pp 1799–1808.